TURBULENT BOUNDARY LAYERS OVER HETEROGENEOUS RIDGES AT HIGH REYNOLDS NUMBERS

Takfarinas Medjnoun, Mattias Nilsson-Takeuchi and Bharathram Ganapathisubramani
Department of Aeronautics and Astronautics
University of Southampton
Burgess Road, Southampton SO17 1BJ, Hampshire, UK
t.medjnoun / m.nilsson / g.bharath@soton.ac.uk@soton.ac.uk

ABSTRACT

The mean and turbulent flow characteristics of a nominally-zero pressure gradient turbulent boundary layer developing over a smooth spanwise-ridge heterogeneous surface are examined experimentally. The impact of surface heterogeneity on drag, flow topology, and spectral characteristics is investigated across a range of Reynolds numbers. The results indicate that frictional drag remains dependent on Reynolds number for $S/\delta \sim O(1)$, where S and δ represent the spanwise spacing between two adjacent ridges and the spanwise-averaged boundary layer thickness, respectively. However, for $S/\delta < 1$, there is an indication of Reynolds number invariance, suggesting a possible existence of an equivalent sandgrain roughness height k_s. The analysis of the flow field results reveals that the significance of secondary motions remains largely influenced by S/δ but is also sensitive to the relative roughness height h/δ rather than the roughness Reynolds number h^+, when compared with our previous study (Medjnoun *et al.*, 2020). Examination of the premultiplied energy spectra of the streamwise velocity fluctuations shows that secondary motions exert different levels of influence across a wide range of scales and throughout a large portion of the turbulent boundary layer. Specifically, the secondary motions rearrange how energy is redistributed among large scales, preventing naturally occurring very-large-scale motions (VLSMs) above the ridges, which are dominated by upwash motions, while coexisting with VLSMs in the valley for $S/\delta \sim O(1)$.

INTRODUCTION

Despite over a century of research, rough-wall turbulence remains an active and critical area of study. Its significance spans various engineering applications and is compounded by the complex dynamics of rough-wall flow. A persistent question in rough-wall flows revolves around characterizing drag in relation to surface properties and accurately predicting it at full-scale (Chung *et al.*, 2021). While considerable progress has been made in leveraging experimental and numerical resources to investigate various roughness configurations, several important questions remain unanswered.

Currently, conventional predictive tools for drag are built on a framework that assumes homogeneous roughness. However, this assumption proves impractical and inadequate when dealing with surfaces exhibiting patchiness and heterogeneity, as encountered in real-world scenarios. Such surfaces generate large-scale secondary motions (Anderson *et al.*, 2015), resulting in highly three-dimensional turbulent flows characterized by alternating high- and low-momentum pathways (HMPs and LMPs). This renders conventional predictive tools inadequate for many engineering applications. The lack of reliable predictive tools primarily stems from our limited understanding of drag behavior over surfaces exhibiting heterogeneity, particularly since existing literature predominantly covers low to moderate Reynolds numbers. Therefore, to advance and refine our predictive tools, it is crucial to investigate how drag behaves on heterogeneous surfaces at high Reynolds numbers, and whether we can establish an equivalent homogeneous sandgrain roughness height for spanwise heterogeneous surfaces (Hutchins *et al.*, 2023).

Moreover, during the past decade, considerable effort has been devoted to understanding the influence of secondary motions on naturally occurring large and very large-scale motions. For instance, Nugroho *et al.* (2013) investigated the effect of a converging-diverging riblet surface roughness on a turbulent boundary layer, and reported modifications in the distribution of energy among the largest energetic structures. Medjnoun *et al.* (2018) examined turbulent boundary layers over smooth surfaces with longitudinal ridges, and reported dissimilarities in mean and spectral attributes compared to smooth walls. They noted a lack of similarity across all scales in the near-wall region, with gradual recovery at smaller wavelengths for $S/\delta > 1$. Barros *et al.* (2018) studied the structural attributes of a turbulent boundary layer flow over a complex roughness topography, modeled from a turbine blade damaged by foreign material deposition. Their findings revealed significant variations in spectral content across the spanwise location of the surface, with energy redistribution from longer to shorter wavelengths at the LMPs, while no significant changes were observed at the HMP.

More recently, Zampiron *et al.* (2020) explored the interrelation between secondary motions and the very large-scale motions in an open channel flow over streamwise ridges. Their results showed that for $S/\delta < 1$, VLSMs are entirely suppressed, suggesting that secondary motions prevent their formation by absorbing their energy, with the secondary motions themselves manifesting at lower wavelengths compared to the VLSMs. Finally, Wangsawijaya & Hutchins (2022) investigated the unsteady nature of secondary motions alongside large-scale structures in turbulent boundary layers over spanwise heterogeneous roughness. Their results supported the findings of Zampiron *et al.* (2020), showing that secondary motions exhibit a meandering character and are maximised when $S/\delta \sim O(1)$. They also demonstrated that secondary motions and large-scale structures coexist in the limits of $S/\delta >> 1$ and $S/\delta << 1$.

Despite the valuable insights gained from these recent studies, it is important to note that they are primarily conducted at low to moderate Reynolds numbers. Therefore, the true nature of influence and interaction between secondary flows and very large-scale motions remains largely unexplored. Addressing these questions has the potential to significantly enhance our understanding, not only of heterogeneous rough-wall flows but also of rough-wall-bounded turbulence in general. Hence, high Reynolds number experiments and/or simulations, along with modeling techniques, could prove beneficial for the various lines of inquiry mentioned above. In this study, we present an experimental investigation of topography-induced secondary flows in high Reynolds number turbulent boundary layers. The drag of these heterogeneous surfaces is assessed using an in-house Floating-Element Drag Balance (FEDB). Flow topology is examined using stereoscopic Particle Image Velocimetry (sPIV), while turbulence spectral characteristics are investigated using Hot-Wire Anemometry (HWA).

EXPERIMENTAL METHODS

The measurement campaign was conducted in the Boundary Layer Wind Tunnel (BLWT) at the University of Southampton. The BLWT is a closed-loop Göttingen-type tunnel, featuring a 12 m long test section in the x-direction, with a cross-section of 1 m × 1.2 m in the wall-normal and spanwise directions (in the y,z-plane), respectively. The BLWT includes a cooling unit to maintain a constant air temperature within a range of ± 0.1°C inside the flow loop, achieved using two heat exchangers and a PID temperature controller. The free-stream velocity (U_∞) can reach up to 50 m/s, with a turbulence intensity level of 0.1%. A schematic describing the surface arrangement along with the different experimental methods employed is illustrated in Figure 1.

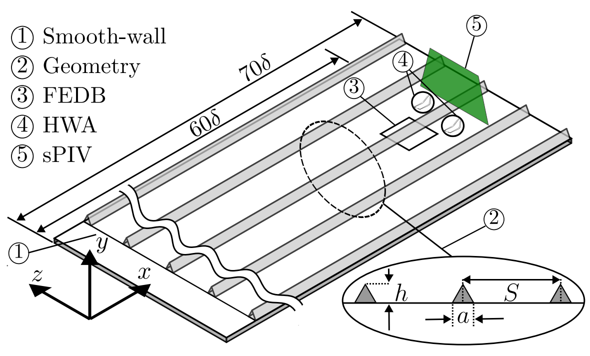

Figure 1. Schematic of the spanwise-heterogeneous ridge-type surface and illustration of the experimental methods featuring the FEDB, HWA, and sPIV setups.

Surface heterogeneity

The surface heterogeneity consists of a smooth base surface onto which longitudinal triangular ridges, similar to the HS2 surface investigated by Medjnoun *et al.* (2020), are affixed. The rods are equilateral triangles with a side length of $a = 6.4$ mm and a height of $h = 5.6$ mm. These ridges are arranged at three different spanwise spacings: S = 50 mm, 100 mm, and 200 mm, labeled T50, T100, and T200, respectively. They are nominally equivalent to $S/\delta \approx 0.3, 0.6$, and 1.3, respectively, and $h/\delta \approx 4\%$, when scaled with the spanwise-averaged boundary layer thickness δ.

Drag Balance

The wall shear stress is directly measured using an in-house FEDB. Its design is based on a zero-displacement force-feedback system (see Aguiar Ferreira *et al.* (2024) for further details). The floating element is a 200-mm-side square, flush-mounted with the wind tunnel floor, approximately 60 δ from the inlet. To determine the frictional drag C_f as a function of Reynolds number and examine the possible existence of an aerodynamic roughness length scale for such surfaces, the FEDB is subjected to a series of nine free-stream velocities ranging from 10 to 45 m/s. Each acquisition lasted 120 s and was sampled at 256 Hz, equivalent to 2500 boundary-layer eddy turnover times ($\tau_{eddy} = \delta/U_\infty$) at the lowest operating speed, with a total of five repetitions per velocity. Pre- and post-calibrations were conducted for each configuration, with a change in the calibration coefficient of less than 0.5%.

Particle Image Velocimetry

The flow is examined in the cross-plane (y,z) using sPIV at roughly the same station as in the FEDB measurements. The flow is traced by vaporized glycerol-water particles and then illuminated with a laser light sheet generated by a two-pulse laser operating at 250 mJ. An optical system for beam focus/expansion of the light sheet is used to obtain a uniform 1.5 mm thickness measurement plane. Particle images are recorded by two 25 MP sCMOS cameras fitted with 100 mm lenses and mounted on Scheimpflug adapters, which correct for the oblique view angle (±45°) by adjusting the focal plane. A double-plane calibration target aligned with the light sheet is used to determine the mapping function for each camera, using a third-order polynomial fit. This resulted in a Field-of-View (FOV) of $2\delta \times 2\delta$ in the (y,z)-plane.

Convergence in the first and second-order statistics is achieved by acquiring 3000 statistically independent image pairs at three speeds: $U_\infty = 10, 20$, and 30 m/s. The velocity vector fields are subsequently obtained using a decreasing multipass scheme, starting from 64 pixels × 64 pixels interrogation windows down to 24 pixels × 24 pixels with a 50% overlap, resulting in an effective vector spacing of 1 mm.

Hot-Wire Anemometry

Two single hot-wire boundary layer-type probes are used to simultaneously measure the time series of the streamwise velocity at the two symmetry planes: $z/S = 0$ and $z/S = 0.5$. Measurements were acquired at a similar location as the FEDB, at four speeds: $U_\infty = 10, 20, 30$, and 40 m/s, using a DANTEC Streamline Pro CTA system. The flow is logarithmically traversed at 50 wall-normal locations, with each point being recorded for 3 to 10 minutes (depending on U_∞) and sampled at 60 kHz (and low-pass filtered at 30 kHz). These durations amount to 25,000 boundary-layer eddy turnover times, allowing the convergence of the streamwise turbulence intensity and spectra. Pre- and post-calibrations were conducted to correct for temperature and electrical drifts, which were found to be less than 1%.

RESULTS AND DISCUSSION

Frictional drag

The results from the FEDB are illustrated in Figure 2, depicting the response of the wall shear stress to changes in the spanwise spacings of the surface heterogeneity.

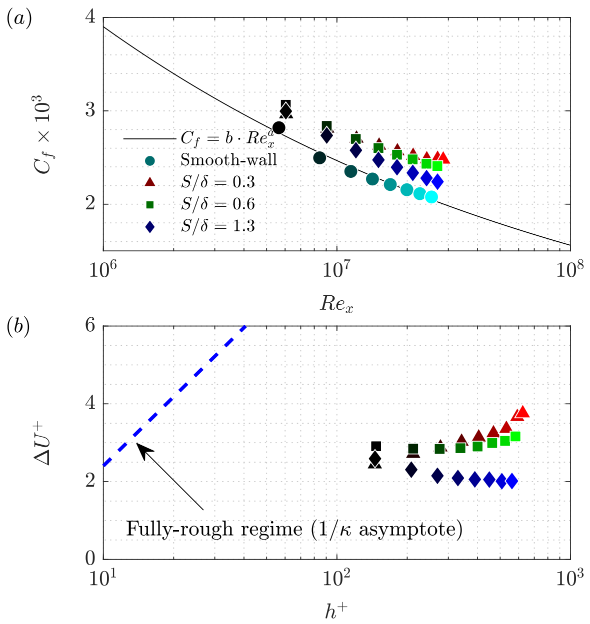

Figure 2. (a) Variation of the skin-friction coefficient as a function of Reynolds number, compared with the smooth-wall baseline and Schlichting power law, and (b) the associated roughness function. The blue dashed line represents the classical 'homogeneous' fully-rough regime, with a $1/\kappa$ asymptote.

Figure 2(a) illustrates the variation of the skin-friction coefficient C_f as a function of Re_x. At low Reynolds numbers, there is no clear distinction between the three surfaces. However, as Re_x increases, a proportional difference begins to manifest (around $Re_x \approx 10^7$). At the highest measured Reynolds number (approximately $Re_x \approx 3 \times 10^7$), T50 exhibits the highest frictional drag, followed by T100 and then T200, respectively. This outcome is expected since T50 has a larger surface area compared to T100 and T200 (where C_f scales proportionally with the planform solidity). However, the drag increase relative to the smooth wall at the highest Reynolds number does not exceed 25% (for T50).

The results also indicate the decay rate of C_f, with T50 possibly reaching the beginning of an asymptote, as the last three measurement points remain relatively constant. This Reynolds number invariance suggests the possible existence of a fully-rough regime; however, it is likely that this regime differs from the classical homogeneous fully-rough one, mainly due to the presence of secondary flows. Conversely, the other two surfaces, T100 and T200, clearly exhibit a decaying skin-friction coefficient, indicating that they are still in what could be termed as a transitionally-rough regime.

The differences in frictional drag between the rough and smooth surfaces can be quantified using the roughness function:

$$\Delta U^+ = \sqrt{\frac{2}{C_f^S}} - \sqrt{\frac{2}{C_f^R}}, \tag{1}$$

at matched frictional Reynolds numbers Re_τ (for further details, see Medjnoun *et al.* (2023)). Figure 2(b) illustrates that the roughness function remains relatively low compared to classical rough-wall flows, with ΔU^+ ranging from 2 to 4 at the highest Reynolds number. Although these values are relatively low for such Reynolds numbers, they are not surprising, as these surfaces lack pressure drag-producing features, which are the primary source for drag (pressure drag) in fully-rough regimes. However, the variation of $\Delta U^+ = f(h^+)$ for T50 (and to a lesser extent T100) is observed to begin following the $1/\kappa$ asymptote, suggesting a possible existence of an equivalent k_s. Nonetheless, this behavior remains unclear for T200, even at higher Reynolds numbers, therefore warrants further investigation.

Flow topology

Figure 3(a) displays the normalized mean streamwise velocity map for the different surfaces at approximately $Re_\tau \approx 10^4$, compared with the smooth wall. To emphasize the difference in spanwise wavelength, the maps are cropped in the z-direction to include only one spanwise wavelength, delineated using vertical blue dashed lines. Consistent with previous studies, a noticeable difference in the mean flow can be observed, manifesting in the form of alternating HMPs and LMPs. The degree of spanwise heterogeneity appears to vary across cases and is highest around $S/\delta \sim O(1)$, which is in agreement with existing literature (Mejia-Alvarez & Christensen, 2013; Nugroho *et al.*, 2013; Barros & Christensen, 2014; Vanderwel & Ganapathisubramani, 2015).

Interestingly, the significance of the heterogeneity appears to be relatively weaker compared to the findings of Medjnoun *et al.* (2020). These differences are qualitatively more evident when examining the normalized vorticity-signed swirling strength ($\lambda_{ci}\delta/U_\infty$) maps shown in Figure 3(b). The results indicate that each ridge is accompanied by a pair of streamwise rolling modes, whose intensity and size diminish and increase, respectively, as S/δ increases. This suggests that at low $S/\delta < 1$, the surface heterogeneity produces smaller but stronger (more intense) secondary motions, which have a higher mixing potential. In contrast, cases where $S/\delta \sim O(1)$ generate larger but weaker secondary motions, with a lower potential for mixing, hence leading to a higher degree of heterogeneity.

Furthermore, the difference in the significance of secondary motions between the present study and that of Medjnoun *et al.* (2020) is believed to stem from the difference in h/δ, which currently stands at 4%, compared to 10% in the previous study. This distinction is also evident when examining the vorticity-signed swirling strength map in both studies, which shows that secondary motions currently occupy up to a maximum of half of δ, contrasting with the consistent two-thirds observed in the previous study. It's worth noting that despite the difference in Re_τ between both studies (3000 and 10000 in the previous and present work, respectively), the ridge height inner-scaled h^+ is approximately matched (300 and 400 in the previous and current works, respectively). This indicates that the secondary motions are more sensitive to h/δ rather than h^+.

To quantify the overall impact of the secondary motions on the turbulent boundary layer flow, the spanwise-averaged total shear stress ($\langle \overline{\tau_{xy}} \rangle = \mu \langle \frac{dU}{dy} \rangle - \langle \overline{uv} \rangle - \langle \tilde{u}\tilde{v} \rangle$), which represents the sum of the viscous, turbulent, and dispersive components, respectively, is examined in Figure 4. The former component is typically noticeable in the very near-wall region and is negligible beyond the buffer layer, while the latter is present

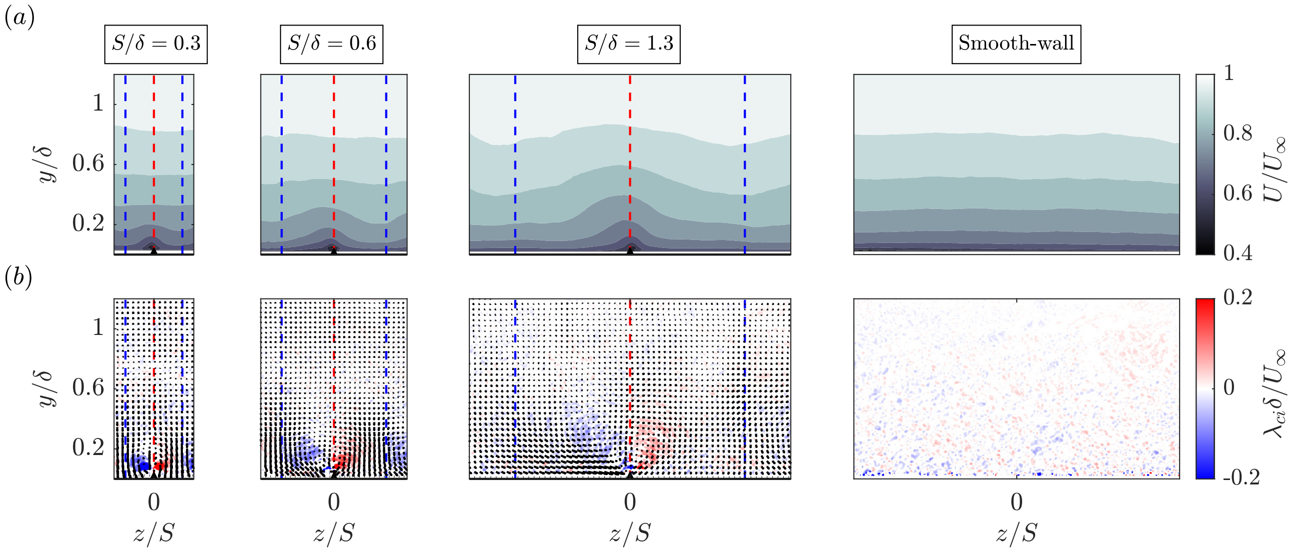

Figure 3. Maps depicting the normalised (*a*) mean streamwise velocity and (*b*) vorticity-signed swirling strength for the various cases. Vertical red- and blue-dashed lines denote a full wavelength at the spanwise locations of the low-momentum pathways (LMPs) and high-momentum pathways (HMPs), respectively, where hot-wire profiles have been collected. Cross-sections of the ridges are provided at the bottom of the maps for scale reference.

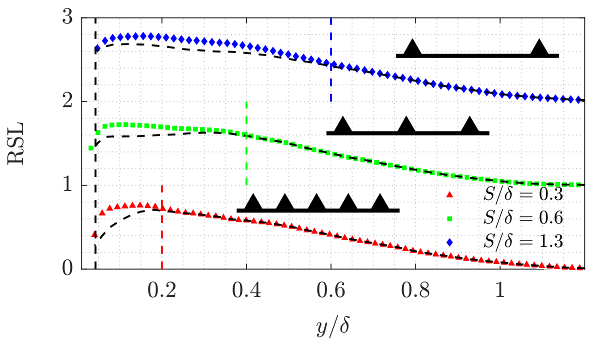

Figure 4. Wall-normal distribution of the spanwise-averaged total shear stress profiles ($\langle\overline{\tau_{xy}}\rangle = \langle\overline{uv}\rangle + \langle\tilde{u}\tilde{v}\rangle$) with their associated turbulent shear stress component (black dashed lines $\langle\overline{uv}\rangle$). Vertical dashed lines delineate the extent of the roughness sublayer (RSL), indicating the height at which $\langle\tilde{u}\tilde{v}\rangle > 0$ for the different cases.

from the wall up to a few roughness heights above the canopy layer, quantifying the roughness sublayer (RSL).

The results, shown in Figure 4, depict the total shear stress highlighted with colored symbols, whereas the turbulent stress is represented with the black dashed line. The findings indicate that the wall-normal height at which the total and turbulent stresses are spanwise heterogeneity-free (i.e., $\langle\tilde{u}\tilde{v}\rangle = 0$ and $\langle\overline{\tau_{xy}}\rangle = \langle\overline{uv}\rangle$) increases as a function of S/δ, owing to the increase in significance of the secondary motions. However, their intensity proportionally decreases as their size increases, believed to be caused by the fact that smaller-sized secondary motions tend to increase spanwise mixing due to their high intensity, leading to a weaker heterogeneity. These observations also corroborate findings from previous research, such that the spanwise wavelength of the surface remains a fundamental scaling parameter for the secondary motions, but additionally highlight the importance of h/δ, which cannot be neglected when comparing the significance of secondary flows induced by ridge-type heterogeneous surfaces.

Spectral characteristics

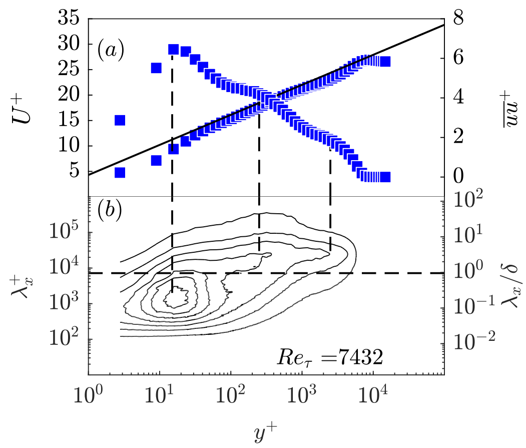

Figure 5. (*a*) Wall-normal distribution of the mean streamwise velocity and variance profiles scaled in inner units and (*b*) its associated one-dimensional premultiplied energy spectra $k_x\phi_{xx}/U_\tau^2$. These profiles are measured at the valley symmetry plane for the T100 case. The vertical dashed lines depict the signatures of the different turbulence structures.

To explore the impact of surface heterogeneity and secondary flows on the turbulent boundary layer, spectral analysis of streamwise velocity fluctuations is conducted on the HWA data at both symmetry planes. Figure 5 illustrates the inner-normalized profiles of the mean and variance, along with a contour map of the premultiplied energy spectra $k_x\Phi_{xx}/U_\tau^2$, where k_x represents the streamwise wavenumber.

Figure 5(*a*) illustrates results obtained at the valley symmetry plane (HMP) for the T100 case ($S/\delta = 0.6$). Despite the spanwise heterogeneity of the surface, the local profile still exhibits a logarithmic distribution in the mean flow. Moreover, the streamwise variance profile reveals a distinct near-wall turbulence intensity peak at $y^+ \approx 15$, a characteristic commonly

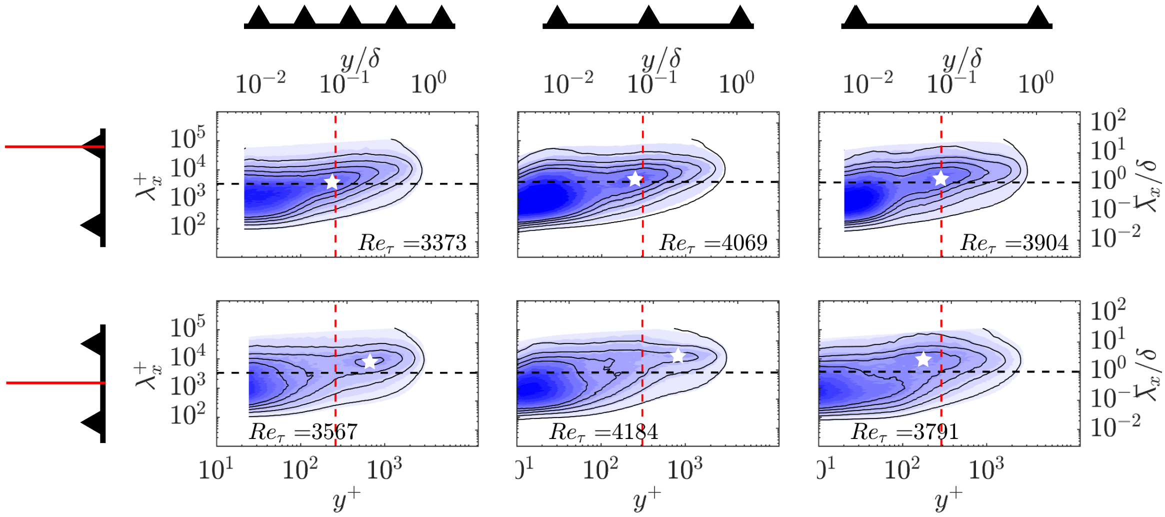

Figure 6. Premultiplied streamwise energy spectrograms for the three spacings at both symmetry planes. The horizontal black dashed lines mark the wavelength $\lambda_x \approx \delta$, and the vertical red dashed lines denote the wall-normal location of the geometrical center of the logarithmic region. The white starts depict the signatures of the secondary motions, whereas the red stars depict the signatures of the VLSMs.

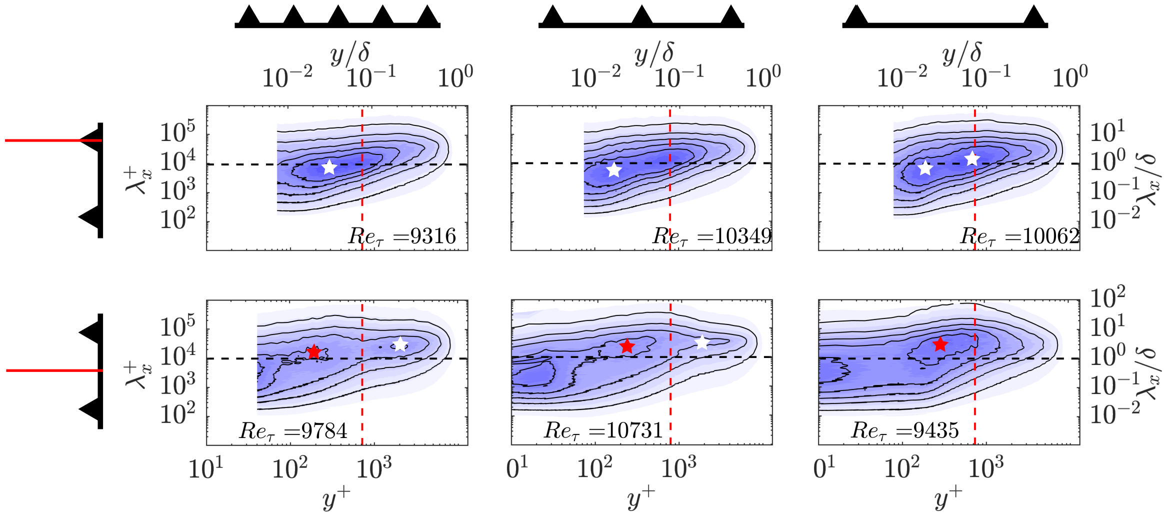

Figure 7. Same as above at high Reynolds number.

observed in turbulent flows over smooth surfaces. This peak is indicative of the near-wall structure associated with low-speed streaks, with a characteristic length scale of $\lambda_x^+ \approx 1000$, as depicted in figure 5(*b*). This near-wall streak cycle is well-documented as the primary source of turbulence production in wall-bounded flows over smooth surfaces (Jiménez & Pinelli, 1999).

Additionally, the logarithmic region reveals a plateau at a wall-normal height lower but close to the geometric center of the overlap region, likely indicating the emergence of Very Large-Scale Motions (VLSMs) given their characteristic length scale $\lambda_x/\delta \approx 3$–4, which are anticipated at such Reynolds numbers ($Re_\tau \approx 7500$). Moving further into the outer region (at $y^+ \approx 2500 \equiv y/\delta \approx 0.3$), another plateau emerges, possibly resulting from an interaction between the naturally occurring VLSMs and the artificially generated secondary motions. However, further examination of spectral maps at both symmetry planes (HMPs and LMPs) for various cases, as well as across a range of Reynolds numbers, is needed to highlight any evidence of the effects of secondary motions on energy redistribution across different length scales.

Spectrograms for the different spacings (T50, T100, and T200) at $Re_\tau \approx 3500$–4000 are presented in Figure 6. The figure displays spectral maps for each spacing in columns and the spanwise locations in rows. Horizontal black dashed lines indicate the cutoff wavelength between small and large scales (i.e., $\lambda_x \approx \delta$), while vertical red dashed lines denote the wall-normal location of the geometric center of the logarithmic region, where VLSM signatures are anticipated.

Comparison of the spectra above the ridge (first row) across cases reveals that the spectra in the near-wall region still exhibit signatures of the near-wall streak cycle. However, there might be a possible alteration in the wall-normal location at which it occurs ($y^+ > 15$), potentially due to the mean upwash induced by the secondary motions. It is worth noting that the ridge spectral maps have been scaled with a local origin, i.e., the local origin is set at the tip of the ridge ($y_{origin} = h$). If the maps were presented with a global origin (i.e., $y_{origin} = 0$ at the valley), the spectra would be shifted farther away from the wall, making visual assessment impractical. Hence, using this local origin, changes in the spectra in the vicinity of the ridge are clearer and more distinguishable.

Moving farther away from the wall, a local energetic peak begins to emerge, closely located around the geometric center of the logarithmic region. However, this spectral peak seems to occur at a lower wavelength ($\lambda_x \approx 1.5\delta$) compared to the VLSMs. This observation remains consistent across the three cases and becomes more distinguishable as S/δ increases. This suggests that this length scale is likely associated with the emergence of the secondary motions.

In contrast, the spectral maps measured at the valley symmetry plane (second row) suggest that the near-wall peak may have shifted downward due to the common downwash occurring between the ridges, leading to the HMP. Moving farther away, at the geometric center of the logarithmic region, no distinguishable evidence of the imprint of VLSMs can be observed across the different cases. However, at a greater distance from the wall ($y/\delta \approx 0.2$–0.3), a noticeable local spectral peak emerges with a wavelength of approximately $\lambda_x \approx 3$–4δ. Although this observation could be interpreted as the emergence of the VLSMs, being somehow pushed away from the log region due to the influence of secondary motions, it should be noted that the Reynolds number remains relatively low to observe any imprint of the VLSMs at $Re_\tau \approx 3500$–4000. Therefore, it is more plausible to assume that these new energetic length scales are associated with the manifestation of secondary motions rather than being caused by the VLSMs. In fact, further evidence can be observed when examining the high Reynolds number cases.

Similarly to Figure 6, Figure 7 displays the same spectral maps but at higher Reynolds numbers ($Re_\tau \approx 9500$–10500). Interestingly, the results indicate that above the ridge, the near-wall peak shifted even farther away to the point where it has merged with the previously observed outer spectral peak for the $S/\delta = 0.3$ and 0.6 cases. This observation holds true for the $S/\delta = 1.3$ case as well, albeit to a lesser extent, where the outer spectral peak can still be observed. These findings reveal that at high Reynolds numbers, the secondary motions at the LMP significantly alter the turbulence structure and the way energy is distributed among different length scales, impacting both the near-wall streak cycle and preventing the naturally occurring VLSMs.

Above the valley, on the other hand, the secondary motions seem to coexist with both the near-wall peak and what appears to be the re-emerging VLSM peak (highlighted with the red star in the second row of Figure 7). Interestingly, the re-emergence of the VLSM peak starts from the near-wall region at lower wavelengths for $S/\delta = 0.3$ and increases for $S/\delta = 0.6$, until another interaction between the VLSMs and the secondary flow peaks is observed for $S/\delta = 1.3$, forming a new energetic peak albeit at a slightly lower location than the geometric center of the log region. This suggests that secondary motions exert varying levels of influence on the VLSMs in different regions of the topography.

In summary, our findings reveal that secondary motions play a crucial role in altering turbulence near ridges, especially affecting the occurrence of VLSMs, particularly evident at higher Reynolds numbers. Moreover, secondary motions can intricately coexist with both near-wall turbulence and re-emerging VLSMs, under certain conditions of S/δ, revealing the complex interaction between these phenomena.

REFERENCES

Aguiar Ferreira, M, Costa, P & Ganapathisubramani, B 2024 Wall shear stress measurement using a zero-displacement floating-element balance. *Exp Fluids* **65** (4), 56.

Anderson, W., Barros, J. M., Christensen, K. T. & Awasthi, A. 2015 Numerical and experimental study of mechanisms responsible for turbulent secondary flows in boundary layer flows over spanwise heterogeneous roughness. *J. Fluid Mech* **768**, 316–347.

Barros, J. M. & Christensen, K. T. 2014 Observations of turbulent secondary flows in a rough-wall boundary layer. *J. Fluid Mech* **748**.

Barros, J. M., Schultz, M. P. & Flack, K. A. 2018 Measurements of skin-friction of systematically generated surface roughness. *International Journal of Heat and Fluid Flow* **72**, 1–7.

Chung, D., Hutchins, N., Schultz, M. P. & Flack, K. A. 2021 Predicting the drag of rough surfaces. *Ann. Rev. Fluid Mech.* **53**, 439–471.

Hutchins, N, Ganapathisubramani, B, Schultz, MP & Pullin, DI 2023 Defining an equivalent homogeneous roughness length for turbulent boundary layers developing over patchy or heterogeneous surfaces. *Ocean Eng.* **271**, 113454.

Jiménez, Javier & Pinelli, Alfredo 1999 The autonomous cycle of near-wall turbulence. *J. Fluid Mech.* **389**, 335–359.

Medjnoun, T., Aguiar Ferreira, M., Reinartz, R., Nugroho, B., Monty, J., Hutchins, N. & Ganapathisubramani, B. 2023 Assessment of aerodynamic roughness parameters of turbulent boundary layers over barnacle-covered surfaces. *Exp Fluids* **64** (11), 169.

Medjnoun, T., Vanderwel, C. & Ganapathisubramani, B. 2018 Characteristics of turbulent boundary layers over smooth surfaces with spanwise heterogeneities. *J. Fluid Mech* **838**, 516–543.

Medjnoun, T., Vanderwel, C. & Ganapathisubramani, B. 2020 Effects of heterogeneous surface geometry on secondary flows in turbulent boundary layers. *J. Fluid Mech* **886**.

Mejia-Alvarez, R. & Christensen, K. T. 2013 Wall-parallel stereo particle-image velocimetry measurements in the roughness sublayer of turbulent flow overlying highly irregular roughness. *Phys. Fluids* **25** (11), 115109.

Nugroho, B., Hutchins, N. & Monty, J. P. 2013 Large-scale spanwise periodicity in a turbulent boundary layer induced by highly ordered and directional surface roughness. *Intl J. Heat Fluid Flow* **41**, 90–102.

Vanderwel, C. & Ganapathisubramani, B. 2015 Effects of spanwise spacing on large-scale secondary flows in rough-wall turbulent boundary layers. *J. Fluid Mech* **774**, R2.

Wangsawijaya, Dea Daniella & Hutchins, Nicholas 2022 Investigation of unsteady secondary flows and large-scale turbulence in heterogeneous turbulent boundary layers. *Journal of Fluid Mechanics* **934**, A40.

Zampiron, Andrea, Cameron, Stuart & Nikora, V 2020 Secondary currents and very-large-scale motions in open-channel flow over streamwise ridges. *Journal of Fluid Mechanics* **887**, A17.